

REPORT DOCUMENTATION PAGE

The public reporting burden for this collection of information is estimated to average 1 hour per response, including the time for reviewing instructions, searching existing data sources, gathering and maintaining the data needed, and completing and reviewing the collection of information. Send comments regarding this burden estimate or any other aspect of this collection of information, including suggestions for reducing the burden, to the Department of Defense, Executive Service Directorate (0704-0188). Respondents should be aware that notwithstanding any other provision of law, no person shall be subject to any penalty for failing to comply with a collection of information if it does not display a currently valid OMB control number.

PLEASE DO NOT RETURN YOUR FORM TO THE ABOVE ORGANIZATION.

1. REPORT DATE (DD-MM-YYYY) 09-03-2009		2. REPORT TYPE Final		3. DATES COVERED (From - To) March 2006 - March 2009	
4. TITLE AND SUBTITLE Next Generation Image Restoration for Space Situational Awareness				5a. CONTRACT NUMBER	
				5b. GRANT NUMBER FA9550-06-1-0179	
				5c. PROGRAM ELEMENT NUMBER	
6. AUTHOR(S) Jefferies, Stuart, M. Hope, Douglas, A.				5d. PROJECT NUMBER	
				5e. TASK NUMBER	
				5f. WORK UNIT NUMBER	
7. PERFORMING ORGANIZATION NAME(S) AND ADDRESS(ES) University of Hawaii/Institute for Astronomy 34 Ohia Ku St., Pukalani, Hawaii 96768-8288				8. PERFORMING ORGANIZATION REPORT NUMBER	
9. SPONSORING/MONITORING AGENCY NAME(S) AND ADDRESS(ES) Air Force Office of Scientific Research 875 N Randolph St Arlington, VA 22203 Dr. Kent Miller/NE				10. SPONSOR/MONITOR'S ACRONYM(S)	
				11. SPONSOR/MONITOR'S REPORT NUMBER(S)	
12. DISTRIBUTION/AVAILABILITY STATEMENT Approved for Public Release					
13. SUPPLEMENTARY NOTES					
14. ABSTRACT <p>The imaging of Earth-orbiting objects using large aperture telescopes equipped with adaptive optics is a critical component of Space Situational Awareness. Unfortunately, due to limitations in the adaptive optics, compensation of the wave-front distortions imparted by the Earth's turbulent atmosphere is incomplete. Achieving the quality of imagery necessary for high confidence monitoring of the near space environment, therefore requires the use of image restoration methods to remove the uncorrected component of the image blur.</p> <p>We have developed a novel blind image restoration algorithm for use with data obtained under a wide range of imaging modalities, including "long-exposure" diversity imaging. By capitalizing on new forms of prior information, and improving the synergy between the data acquisition and image restoration processes, we have significantly extended the observing conditions under which we can produce high-fidelity restorations with a high dynamic range. These improvements enable two new capabilities for the Air Force's 3-meter class telescopes: the imaging of faint targets, such as micro-satellites in geosynchronous orbit, and imaging through strong atmospheric turbulence.</p>					
15. SUBJECT TERMS Blind Deconvolution, Image Restoration, Temporal Phase Diversity, Wavelength Diversity, Spectral Holes					
16. SECURITY CLASSIFICATION OF:			17. LIMITATION OF ABSTRACT UU	18. NUMBER OF PAGES 15	19a. NAME OF RESPONSIBLE PERSON Stuart M. Jefferies
a. REPORT U	b. ABSTRACT U	c. THIS PAGE U			19b. TELEPHONE NUMBER (Include area code) 808 573 9520

INSTRUCTIONS FOR COMPLETING SF 298

1. REPORT DATE. Full publication date, including day, month, if available. Must cite at least the year and be Year 2000 compliant, e.g. 30-06-1998; xx-06-1998; xx-xx-1998.

2. REPORT TYPE. State the type of report, such as final, technical, interim, memorandum, master's thesis, progress, quarterly, research, special, group study, etc.

3. DATES COVERED. Indicate the time during which the work was performed and the report was written, e.g., Jun 1997 - Jun 1998; 1-10 Jun 1996; May - Nov 1998; Nov 1998.

4. TITLE. Enter title and subtitle with volume number and part number, if applicable. On classified documents, enter the title classification in parentheses.

5a. CONTRACT NUMBER. Enter all contract numbers as they appear in the report, e.g. F33615-86-C-5169.

5b. GRANT NUMBER. Enter all grant numbers as they appear in the report, e.g. AFOSR-82-1234.

5c. PROGRAM ELEMENT NUMBER. Enter all program element numbers as they appear in the report, e.g. 61101A.

5d. PROJECT NUMBER. Enter all project numbers as they appear in the report, e.g. 1F665702D1257; ILIR.

5e. TASK NUMBER. Enter all task numbers as they appear in the report, e.g. 05; RF0330201; T4112.

5f. WORK UNIT NUMBER. Enter all work unit numbers as they appear in the report, e.g. 001; AFAPL30480105.

6. AUTHOR(S). Enter name(s) of person(s) responsible for writing the report, performing the research, or credited with the content of the report. The form of entry is the last name, first name, middle initial, and additional qualifiers separated by commas, e.g. Smith, Richard, J, Jr.

7. PERFORMING ORGANIZATION NAME(S) AND ADDRESS(ES). Self-explanatory.

8. PERFORMING ORGANIZATION REPORT NUMBER. Enter all unique alphanumeric report numbers assigned by the performing organization, e.g. BRL-1234; AFWL-TR-85-4017-Vol-21-PT-2.

9. SPONSORING/MONITORING AGENCY NAME(S) AND ADDRESS(ES). Enter the name and address of the organization(s) financially responsible for and monitoring the work.

10. SPONSOR/MONITOR'S ACRONYM(S). Enter, if available, e.g. BRL, ARDEC, NADC.

11. SPONSOR/MONITOR'S REPORT NUMBER(S). Enter report number as assigned by the sponsoring/monitoring agency, if available, e.g. BRL-TR-829; -215.

12. DISTRIBUTION/AVAILABILITY STATEMENT. Use agency-mandated availability statements to indicate the public availability or distribution limitations of the report. If additional limitations/ restrictions or special markings are indicated, follow agency authorization procedures, e.g. RD/FRD, PROPIN, ITAR, etc. Include copyright information.

13. SUPPLEMENTARY NOTES. Enter information not included elsewhere such as: prepared in cooperation with; translation of; report supersedes; old edition number, etc.

14. ABSTRACT. A brief (approximately 200 words) factual summary of the most significant information.

15. SUBJECT TERMS. Key words or phrases identifying major concepts in the report.

16. SECURITY CLASSIFICATION. Enter security classification in accordance with security classification regulations, e.g. U, C, S, etc. If this form contains classified information, stamp classification level on the top and bottom of this page.

17. LIMITATION OF ABSTRACT. This block must be completed to assign a distribution limitation to the abstract. Enter UU (Unclassified Unlimited) or SAR (Same as Report). An entry in this block is necessary if the abstract is to be limited.

Next Generation Image Restoration for Space Situational Awareness

AFOSR Grant Number: FA9550-06-1-0179

Executive Summary

The imaging of Earth-orbiting objects using large aperture telescopes equipped with adaptive optics is a critical component of Space Situational Awareness. Unfortunately, due to limitations in the adaptive optics, compensation of the wavefront distortions imparted by the Earth's turbulent atmosphere is incomplete. Achieving the quality of imagery necessary for high confidence monitoring of the near space environment, therefore requires the use of image restoration methods to remove the uncorrected component of the image blur.

We have developed a novel blind image restoration algorithm for use with data obtained under a wide range of imaging modalities, including "long-exposure" diversity imaging. By capitalizing on new forms of prior information (spectral holes), and improving the synergy between the data acquisition and image restoration processes (through using wavelength- and temporal phase-diversity channels), we have significantly extended the observing conditions under which we can produce high-fidelity restorations with a high dynamic range. These improvements enable two new capabilities for the Air Force's 3-meter class telescopes: the imaging of faint targets, such as microsatellites in geosynchronous orbit, and imaging through strong atmospheric turbulence.

People Involved in Research: Dr. S. M. Jefferies, Dr. D. A. Hope and Mrs. C. A. Giebink

Publications:

1. Hope, D. A., Jefferies, S. M. and Giebink, C. 2008, "Imaging Geosynchronous Satellites with the AEOS Telescope", *Proceedings of the Advanced Maui Optical and Space Surveillance Technologies Conference*, held in Wailea, Maui, Hawaii, September 2008, Ed.: S. Ryan, The Maui Economic Development Board, p.E33
2. Hope, D. A., Jefferies, S. M., and Giebink, C. A. 2007, "High-resolution imaging through strong turbulence", in *Advanced Signal Processing Algorithms, Architectures, and Implementations XVII*, Proc. SPIE Vol. 6697, , p.66970C
3. Hope, D. A., Jefferies, S. M., and Giebink, C. A. 2007, "Fourier-constrained blind restoration of imagery obtained in poor imaging conditions", *Proceedings of the Advanced Maui Optical and Space Surveillance Technologies Conference*, held in Wailea, Maui, Hawaii, September 2007, Ed.: S. Ryan, The Maui Economic Development Board, p.E56
4. Hope, D. A. and Jefferies, S. M. 2006, "A new Fourier constraint for multi-frame blind deconvolution of imagery obtained through strong turbulence", *Proceedings of the Advanced Maui Optical and Space Surveillance Technologies Conference*, held in Wailea, Maui, Hawaii, September 2006, Ed.: S. Ryan, The Maui Economic Development Board, p.E26

20090325305

Introduction

Two important capabilities for Space Situational Awareness (SSA) studies with the Air Force's 3-meter class telescopes, are the imaging of faint targets and imaging through strong atmospheric turbulence. The former facilitates the monitoring of the health and safety of the U.S. military and civilian assets in geosynchronous orbit. The latter extends both the spectral range (from the infrared into the visible region), and the range of turbulence conditions under which we can obtain high-quality imagery. It also extends the area of sky that can be monitored.

The foundation for achieving these capabilities lies in the efficient removal of the image blur caused by observing through the Earth's turbulent atmosphere. This is a two-step process. The first step is to reduce the level of image blur and improve the image signal-to-noise ratio (SNR) by employing adaptive optics (AO) in the imaging system. As compensation of the distortions in the incoming wavefront by AO is only ever partial, the second step is to remove the remaining (residual) image blur through digital image restoration. Because the point-spread functions (PSFs) for the residual blur are, at best, poorly known, the algorithm of choice for this restoration is multi-frame blind deconvolution (MFBD), where both the target and the PSFs are estimated [1,2].

The quality of the restored imagery in blind restoration problems, which are typically ill conditioned and ill posed, depends on the amount of prior information used to constrain the restoration. In general, the more information used the better the quality of the restoration. Here we demonstrate the advantage provided by using a physics-based model for the PSF and applying strong constraints on its pupil plane and Fourier plane properties. We show that by doing this, we can significantly extend the dynamic range and spectral region over which we can perform successful blind restoration of imagery obtained under a wide range of imaging modalities; including "long exposure" imaging (i.e. the integration time for the observations, T_{int} , is longer than the atmospheric coherence time, τ_0). The pupil plane constraints come through the use of diversity imaging methods [3, 4], something that has, until now, been reserved for "short-exposure" observations (i.e. $T_{\text{int}} \leq \tau_0$). The Fourier plane constraints come through the use of knowledge of the sources of low spectral power in the observations (which we refer to as "spectral holes").

Temporal Phase Diversity

The amount of diversity in the morphology of the PSFs during a set of observations depends on the level of AO compensation, the integration time, and the wavelength of the observations. The level of "PSF diversity" decreases as the first two quantities increase and the last one decreases. Consequently, although AO compensation and longer integration times can improve the image signal-to-noise ratio (SNR), which is of paramount importance when observing faint targets, they also bring a new challenge from the blind restoration point of view: they produce PSFs that are remarkably similar; especially when observing at the longer wavelengths (see Fig. 1). This similarity weakens the advantage provided by performing a multi-frame restoration, where the separation of the two signals that comprise a measured image (the target and PSF) leverages off the diversity in the PSFs.

In order to overcome this limitation we use a variation of the traditional phase diversity method during the data acquisition [3]: temporal phase diversity. Here we inject a temporally varying phase aberration (magnitude varies in time) into the system (as opposed to a static phase aberration). The effect of such an injected signal is to increase the amount of diversity at the lowest spatial frequencies of the PSF (see Fig. 2).

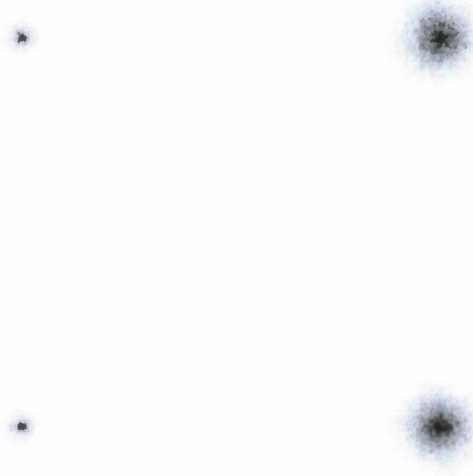


Figure 1. Two separate realizations of an AO-compensated PSF at red ($0.88\ \mu\text{m}$, left) and blue ($0.44\ \mu\text{m}$, right) wavelengths. Here the integration time is 21 times longer than the atmospheric coherence time at the blue wavelength.

However, the cost of this boost in diversity is a reduction in the SNR in the individual data frames due to the sharing of the photons between the data and diversity channels.

We note that when using phase diversity in conjunction with wavelength diversity it may only be necessary to apply the temporal phase diversity method at the longer wavelengths (e.g., if there is sufficient diversity at the shorter wavelengths).

Wavelength Diversity

Current approaches to imaging targets in geosynchronous orbit rely on observations at infrared wavelengths. This is because the level of atmospheric turbulence is less in the infrared than it is at visible wavelengths and AO correction, together with image restoration, is often sufficient to provide high-quality imagery. However, there are a number of reasons why we would like to be able to observe at visible wavelengths. First, the image resolution improves at shorter wavelengths. Second, imaging an object at different wavelengths provides valuable information on the materials present in the target. Third, the target of interest may be a poor reflector at infrared wavelengths; For example, solar cell material, which covers the majority of the surface area of extremely small satellites, has a peak reflectance at blue wavelengths.

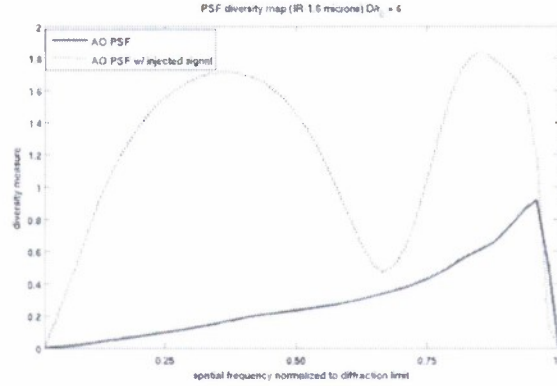


Figure 2. The solid red line denotes the fluctuations (diversity) of the spectra of the AO-PSFs for the scenario $\{T_{in}/\tau_0=21\}$, and the blue dotted line denotes the diversity after injection of a time-varying phase signal (± 1 wave of spherical aberration)

Unfortunately, at shorter wavelengths the coherence length of the atmosphere, as characterized by the Fried parameter r_0 , decreases and the turbulence strength as measured by the ratio D/r_0 (where D is the diameter of the telescope aperture) increases. Eventually the turbulence strength reaches a level ($D/r_0 \sim 25$) where AO compensation and digital image restoration are insufficient to provide the high dynamic range imagery required for faint target detection: thus limiting the spectral range over which we can observe a target. Fortunately, wavelength diversity [4] offers a mechanism to observe targets at shorter wavelengths than would be normally attempted with a large aperture telescope. The underlying principle behind wavelength diversity is straightforward, by observing simultaneously at multiple wavelengths we can capitalize on the fact that the wavefront phases at each wavelength are linked through a common optical path difference [4]. Because of this, observations made at longer wavelengths, where the turbulence conditions are more benign, provide a strong constraint on the low-spatial frequencies of the wavefront phase. This effectively anchors the low spatial frequencies of the wavefront and enables the restoration algorithm to extract the high-spatial frequencies of the wavefront phases from the shorter wavelength observations. Lastly, when using phase-diversity methods, observing simultaneously at multiple wavelengths allows us to inject a different phase aberration at each wavelength, thus further leveraging the phase diversity.

Spectral Holes

An important observable in the spectrum of the data are spatial frequencies that have low Fourier power. Because of the lack of information at these frequencies, we refer to them as *spectral holes*. Spectral holes in the data occur where there are spectral holes in the spectra of both the PSF and object (see Eq. 1.3). Fortunately, it is possible to determine the source of each observed spectral hole in the data. Due to the random nature of the atmospheric turbulence, spectral holes from the PSF will change location with time, while those from the target will remain static. By forming the ensemble spectrum of the data, the spectral holes from the PSFs (which move with time) average out, leaving only those due to the object spectrum. Knowing these it is then straightforward to determine the spectral holes in the data

that come from the atmospheric PSFs (see Fig. 3). This information provides a constraint on the spectra of the estimated object and PSFs. The density of PSF spectral holes increases as D/r_0 increases. At infrared wavelengths, where D/r_0 is small (~ 5 or less), there are very few spectral holes and the effect of applying a PSF spectral hole constraint is minimal. However, when D/r_0 is large (>25) knowledge of the locations of the PSF spectral holes provides a strong constraint on the PSF.

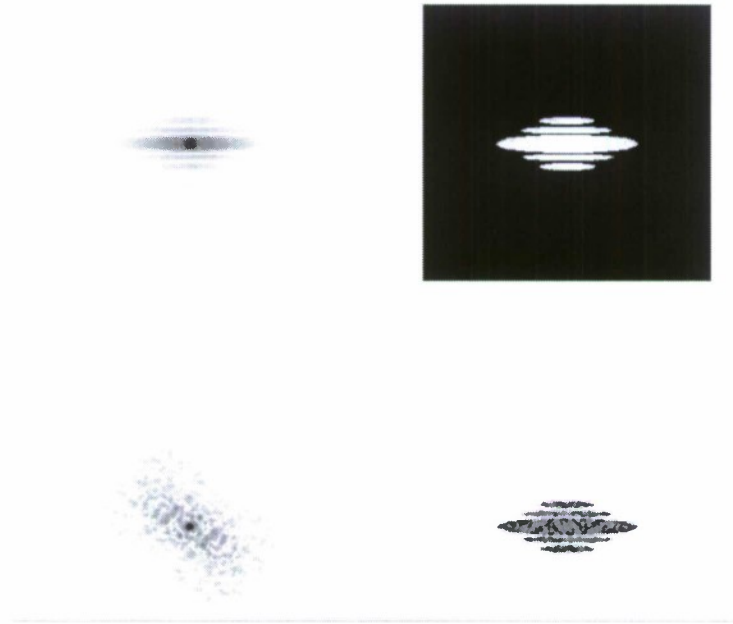


Figure 3. Top Left: Average power spectrum of an ensemble of images of a target observed at $0.4 \mu\text{m}$. Top Right: Binary map where white shows regions of high power in the average power spectrum of the data and the black regions correspond to "object spectral holes". Bottom left: Power spectrum of a PSF used to simulate the observed images. Bottom Right: The product of multiplying the power spectrum of the observation corrupted by the PSF corresponding to the spectrum shown in the bottom left panel, by the binary map in the top right panel. The dark regions show the locations of low spectral power in the PSF ("PSF spectral holes") that are coincident with those of high spectral power in the object.

We note that the value of the PSF spectral hole constraint is diminished (but not negated) when wavefront sensor data are used as a constraint in the restoration process. This is because these data inherently contain the spectral-hole information for the PSFs.

Image Restoration Algorithm

Here we describe our new MFBD restoration algorithm. The algorithm is capable of processing data obtained under a wide variety of imaging modalities including wavelength- and phase-diverse imaging, and "long exposure" imaging.

Modeling the Image Data

We restrict our attention to imagery obtained under isoplanatic conditions, that is, PSFs that are spatially invariant. In this case the target and image intensity distributions, $f(\mathbf{x})$ and $g(\mathbf{x})$, are directly related by the convolution integral

$$g(\mathbf{x}) = \int h(\mathbf{x} - \mathbf{x}') f(\mathbf{x}') d^2 \mathbf{x}'. \quad (1.1)$$

Here, $h(\mathbf{x})$ is the incoherent PSF and the vectors \mathbf{x}, \mathbf{x}' denoting position coordinates in the image and object planes respectively. In practice, we detect and restore the image of the target on a discrete array of pixels, so it is convenient to express Eq. (1.1) as a discrete sum. In addition, as we want to accommodate the restoration of data obtained using the diversity imaging methods, we rewrite Eq. (1.1) as

$$g_{\lambda\varphi k}(\mathbf{x}) = \sum_{\mathbf{x}'} f_{\lambda}(\mathbf{x}') h_{\lambda\varphi k}(\mathbf{x} - \mathbf{x}') + n_{\lambda\varphi k}(\mathbf{x}). \quad (1.2)$$

Here, the subscripts λ, φ, k index the wavelength channel, phase diversity channel and observation timeslot respectively. The function $n_{\lambda\varphi k}(\mathbf{x})$ represents an additive random noise associated with the detection process in each wave/diversity channel. The vectors \mathbf{x}, \mathbf{x}' each denote pixel locations in the image and target intensity distributions. Equivalently, the observed Fourier spectra have the following representation in the Fourier domain,

$$G_{\lambda\varphi k}(\mathbf{u}) = F_{\lambda}(\mathbf{u}) H_{\lambda\varphi k}(\mathbf{u}) + N_{\lambda\varphi k}(\mathbf{u}), \quad (1.3)$$

where the vector \mathbf{u} denotes a discrete spatial frequency. Our MFBD algorithm estimates the target scene at each observation wavelength and the atmospheric PSFs corresponding to each of the wave/diversity channels, such that the predicted model $\hat{g}_{\lambda\varphi k}(\mathbf{x})$ matches the observed data $g_{\lambda\varphi k}(\mathbf{x})$.

PSF Model

We model the incoherent PSF in each wave/diversity channel at timeslot k as,

$$\hat{h}_{\lambda\varphi k}(\mathbf{x}) = \frac{1}{J} \sum_j \hat{a}_{\lambda\varphi jk}^*(\mathbf{x}) \hat{a}_{\lambda\varphi jk}(\mathbf{x}) \begin{cases} J=0 & \text{if } T_{\text{int}} \leq \tau_0 \\ J=\text{int}(T_{\text{int}}/\tau_0)-1, & \text{otherwise} \end{cases} \quad (1.4)$$

where $\hat{a}_{\lambda\varphi jk}(\mathbf{x})$ is the coherent PSF and j indexes its instantaneous realization, and $*$ denotes complex conjugation. The coherent PSF is the inverse Fourier Transform of the complex wavefront in the telescope pupil,

$$\hat{a}_{\lambda\varphi jk}(\mathbf{x}) = \frac{1}{N^2} \sum_{\mathbf{p}} \hat{A}_{\lambda jk}(\mathbf{p}) \exp[-i\hat{\varphi}_{\lambda\varphi jk}(\mathbf{p})] \exp[-2\pi i \mathbf{p} \cdot \mathbf{x}]. \quad (1.5)$$

Here, $\hat{A}_{\lambda jk}(\mathbf{p})$ and $\hat{\phi}_{\lambda \phi jk}(\mathbf{p})$ denote the amplitude and phase of the wavefront, the vector \mathbf{p} denotes a position coordinate in the pupil plane, and N denotes the linear size of the pixel grid. We assume that perturbations in the wavefront amplitude are negligible [8] and thus the amplitude is set to unity inside the pupil.

In each wave/diversity channel, we model the wavefront phase as,

$$\hat{\phi}_{\lambda \phi jk}(\mathbf{p}) = \left(\frac{2\pi}{\lambda} \right) \hat{W}_{jk}(\mathbf{p}) + \psi_{\lambda \phi k}(\mathbf{p}), \quad (1.6)$$

where $\psi_{\lambda \phi k}(\mathbf{p})$ is a certain realization of an injected phase signal during timeslot k and $\hat{W}_{jk}(\mathbf{p})$ denotes the atmospheric optical-path-differences common across all wave channels [4]. The optical path differences at time j in turn are modeled using an orthogonal basis set of functions $\{D_q(\mathbf{p})\}$ defined on a circular domain,

$$\hat{W}_{jk}(\mathbf{p}) = \sum_q \hat{c}_{qjk} D_q(\mathbf{p}), \quad (1.7)$$

where \hat{c}_{qjk} denotes the weight of each function in the basis. We have used Disk Harmonic functions for our basis set, since they behave better near the edges of the pupil than the commonly used Zernike functions [5].

We note that this model for the PSF is extremely versatile and is appropriate for short or long-exposure imagery, with or without phase-/wavelength-diversity data channels. Previously, diversity imaging [4, 5], which puts strong constraints on the wavefront phase, was restricted to short-exposure imagery. Furthermore, with this model for the PSF it is straightforward to incorporate any prior information we may have on the complex wavefront in the pupil (e.g., wavefront sensor data).

Object Model

We model the target scene at wavelength λ using,

$$\hat{f}_\lambda(\mathbf{x}) = \eta_\lambda^2(\mathbf{x}), \quad (1.8)$$

where $\eta_\lambda(\mathbf{x})$ are parameters (pixel intensity values) in the minimization. This parameterization ensures positivity.

Spectral Holes Constraint

We identify spatial frequencies in the data with low Fourier power as *spectral holes*. From an ensemble of data we can distinguish and identify the holes that are due to the spectrum of the target scene and those due to the random atmospheric PSFs

We first identify spectral holes due to the target by computing the signal-to-noise ratio in the ensemble averaged power spectrum of the data,

$$SNR_{\lambda}(\mathbf{u}) = \frac{\langle |G_{\lambda}(u)|^2 \rangle}{\text{var} \{ |G_{\lambda}(u)|^2 \}^{1/2}}. \quad (1.9)$$

Spatial frequencies with a SNR below some threshold value T_F (we used a value of 3) are identified as object spectral holes. A binary mask that identifies these holes is created for each wave channel,

$$M_{\lambda}^F(\mathbf{u}) = \begin{cases} 0, & \text{if } SNR_{\lambda}(\mathbf{u}) \geq T_F \\ 1, & \text{otherwise.} \end{cases} \quad (1.10)$$

Once the object holes are known, the spectral holes in each data frame due to the atmospheric PSF are identified at frequencies where $M_{\lambda}^F(\mathbf{u}) = 0$, by computing for each frame the ratio of the image power spectrum to the standard deviation of the noise power (computed at spatial frequencies beyond the diffraction-limit cut-off frequency). A binary mask that identifies the PSF spectral holes is then defined as,

$$M_{\lambda\phi k}^H(\mathbf{u}) = \begin{cases} 0, & \text{if } |G_{\lambda\phi k}(\mathbf{u})|^2 \geq T_H \sigma_{\lambda\phi} \\ 1, & \text{otherwise} \end{cases} \quad (1.11)$$

where T_H is a threshold parameter (we use a value of 3).

We enforce knowledge of the target spectral holes via the penalty function,

$$\varepsilon_F = \sum_{\lambda} \sum_{\mathbf{u}} M_{\lambda}^F(\mathbf{u}) |\hat{F}_{\lambda}(\mathbf{u})|^2. \quad (1.12)$$

In addition to providing a constraint on the spectrum of the reconstructed object, ε_F also provides a natural regularization on the object as it suppresses noise amplification in regions of low spectral power.

Similarly, we enforce knowledge of PSF spectral holes for each of the wave/diversity channels, via the penalty function,

$$\varepsilon_H = \sum_{\lambda, \phi} \sum_k \sum_{\mathbf{u}} M_{\lambda\phi k}^H(\mathbf{u}) |\hat{H}_{\lambda\phi k}(\mathbf{u})|^2. \quad (1.13)$$

Parameter Estimation

We obtain estimates of the parameters describing the PSFs $\{\hat{c}_{qk}\}$ and the target scene $\{\hat{\eta}_{\lambda}(\mathbf{x})\}$ by using a conjugate gradients algorithm [6] to minimize the error function,

$$\mathcal{E} = \sum_{\lambda, \varphi} \sum_k \sum_{\mathbf{x}} r_{\lambda\varphi k}^2(\mathbf{x}) + \alpha_F \mathcal{E}_F + \alpha_H \mathcal{E}_H \quad (1.14)$$

where

$$r_{\lambda\varphi k}(\mathbf{x}) = m_{\lambda\varphi k}(\mathbf{x}) \times \left(\frac{\hat{g}_{\lambda\varphi k}(\mathbf{x}) - g_{\lambda\varphi k}(\mathbf{x})}{\sqrt{\hat{g}_{\lambda\varphi k}(\mathbf{x}) + \sigma_{\lambda\varphi}^2}} \right). \quad (1.15)$$

Here, $m_{\lambda\varphi k}(\mathbf{x})$ is a binary mask with zeros at locations of bad pixels or pixels with low SNR in the data. The term $\hat{g}_{\lambda\varphi k}(\mathbf{x})$ and $\sigma_{\lambda\varphi}^2$ in the denominator represent the Poisson and Gaussian components of the noise variance, respectively. The parameters α_F and α_H denote scalars that set the strength of the penalty functions in the minimization.

We note that, ideally, the error functions in Eq. (1.14) should mimic probability density functions (i.e. they integrate to unity) so that each term is optimally weighted with respect to the others. However, it is not always practical to achieve this requirement and the weights for each component must be determined that will provide the best solution. Here we have chosen

values for α_H such that the gradient norms $\left| \frac{\partial \mathcal{E}}{\partial c_{qjk}} \right|$ and $\left| \frac{\partial \mathcal{E}_H}{\partial c_{qjk}} \right|$ have close to the same

magnitude at the start of the minimization. In the same manner we chose a value for α_F

such that $\left| \frac{\partial \mathcal{E}}{\partial \eta_{\lambda}(\mathbf{x})} \right|$ and $\left| \frac{\partial \mathcal{E}_F}{\partial \eta_{\lambda}(\mathbf{x})} \right|$ also have equal magnitudes. We have found that this results

in an adequate balancing between fitting the data and enforcing the constraints on spectral holes in the target scene and atmospheric PSF estimates. We have also found that the approach of alternating the minimization between the object and PSF parameters provides a more robust algorithm than when minimizing for both sets of parameters at the same time [9].

We note that although blind image restoration algorithms estimate both the object and the PSFs, they should always be used with the best possible initial estimates for these quantities. For example, for data where $T_{\text{int}} > \tau_0$ it is important that there is some diversity in the initial wavefront phase estimates used for each PSF. Without diversity in the input phases (e.g., using zero phases for the initial guesses) the algorithm falls into a local minimum early on during the minimization. We have found that use of random tip-tilts avoids this problem. For the initial estimate of the object, it is important that there are no areas of low or zero signals where there could conceivably be signal. This is because the parameterization used to enforce positivity inhibits the recovery of signal in areas that are close to zero [10].

Results

Here we demonstrate the performance of our new MFBD algorithm for two cases important for SSA.

1. Imaging Through Strong Turbulence

Here we present restorations of simulated short exposure AO-imagery as would be obtained in strong atmospheric turbulence ($D/r_0=80$). The severity of the image degradation for this level of turbulence, which is at least a factor of three more severe than is typically addressed in the restoration of ground-based imagery, is highlighted in Fig. 4. When running MFBD algorithms on data obtained in this regime of turbulence, the algorithm will typically stagnate due to the plethora of local minima in the parameter space [7]. An example of entrapment in a local minimum that is far from the global minimum is shown on the left in Fig. 5. Steering the algorithm away from the local minima requires the use of prior information: the more information, the better.

Our strategy is to image the object simultaneously at multiple wavelengths, thereby enforcing a common optical path difference constraint on the PSFs, and to enforce the spectral-hole constraint for both the objects (one for each wavelength) and the PSFs. The improvement in image quality when using this approach is demonstrated in the right-hand panel of Fig. 5. This image shows that with sufficient prior knowledge it is possible to extract meaningful information from data that would have otherwise be discarded as “unusable”.

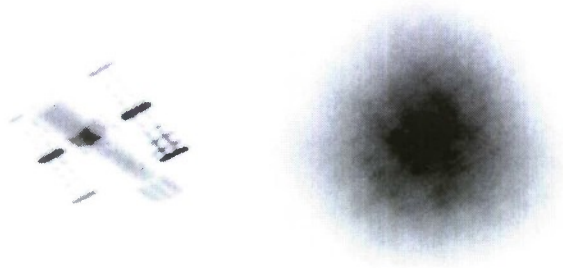


Figure 4. Left: Simulated diffraction-limited, image of the Hubble Space Telescope (HST). Right: Simulated observation of the HST as viewed at $0.4 \mu\text{m}$ with a 3.6m telescope through strong turbulence ($D/r_0 = 80$). The field-of-view here is larger than for the left hand panel. The details of the simulation are provided in the appendix.

This improved ability to restore imagery obtained through strong turbulence conditions means that we are able to dramatically extend both the spectral range (r_0 decreases with decreasing wavelength, consequently D/r_0 is larger at visible wavelengths where r_0 is typically a few centimeters) and the range of turbulence conditions for successfully identification and monitoring of spaced-based targets.



Figure 5. Left: Result of restoration of $D/r_0 = 80$ data shown in Fig. 4 without using spectral-hole information during the restoration process. Right: Result of restoration using spectral holes and observations at to wavelengths ($0.4 \mu\text{m}$ and $1.6 \mu\text{m}$).

II. Imaging Faint Targets

Here we simulated observations of a communications satellite (ANIK-F2) in geosynchronous orbit, as observed with a 3.6m telescope equipped with adaptive optics. The simulations are based on real observations of ANIK-F2 made with the University of Arizona's 6.5 m Multiple Mirror Telescope [11]. To establish our ability to detect extremely faint targets, we have surrounded the communications satellite in our simulation by a number of microsatellites with linear sizes varying between 10cm and 1m. These unresolved targets, whose surfaces are modeled to have the same reflectivity as solar cell material, represent magnitude +14.75 to +11.5 targets, respectively. The full details of the simulation are given in Table 1 in the appendix.

Figure 6 demonstrates how the image quality improves as the level of prior information on the PSFs is increased. The highest quality restoration is obtained when using wavelength- and phase-diverse observations along with wavefront sensing data and PSF spectral holes to constrain the modeling of the PSFs. We find that the temporally varying phase-diversity signal facilitates better estimation of the low spatial frequencies of the target: this is evident in the bottom-right panel of Fig. 6 where the background is cleaner and there are less restoration artifacts than in the top-right and bottom-left panels. We note that there is a cost for including a phase diversity channel, a reduction in the signal-to-noise ratio of the data due to the splitting of the incoming photons between the data and diversity channels. However, as shown in Fig.7 we can compensate for this loss of signal-to-noise ratio by extending the total integration of the observations. Figure 7 shows that with sufficient integration time and the use of diversity imaging methods, we can both obtain a high-resolution image of the primary target and detect several of the microsatellites that would have otherwise remained invisible. Moreover, by observing at multiple wavelengths we garner confirmation of the detection of these micro-satellites.

Discussion

Even at the best observing sites (e.g., Mt. Haleakala), the turbulence conditions can change rapidly with time and prevent high-resolution imaging of targets for a large fraction of the day. In addition, even if the observing conditions are excellent when viewing near zenith, they typically deteriorate quickly as we move away from zenith toward the horizon. Thus, the ability to image through strong turbulence is essential if we are to extend the time and area of sky over which we can successfully identify and monitor space-based targets. Furthermore, with the rapidly growing number of extremely small satellites in orbit, it is becoming more and more important to be able to monitor extremely faint targets, especially foreign satellites that may be in proximity to U.S. assets.

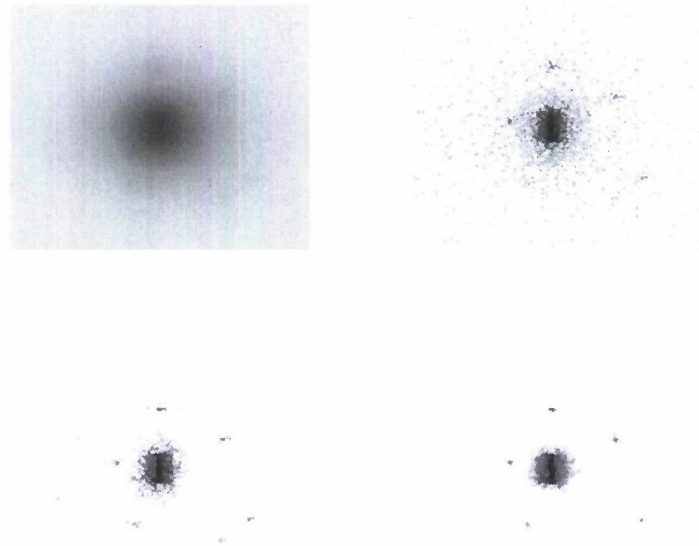


Figure 6. This figure shows the improvements in detection capability when injecting prior information on the wave-front phase into the image restoration process. Top left: mean “long exposure” (3 seconds) image at $0.4\ \mu\text{m}$. Top right: restored image using recorded wave-front sensing (WFS) data. Bottom Left: restored image using WFS data and wavelength diversity (WD) data (i.e. simultaneous observations at $0.4\ \mu\text{m}$ and $1.6\ \mu\text{m}$). Bottom right: restored image using WFS, WD and phase diverse (PD) data (temporally injected ± 1 wave of spherical aberration). The raw AO image tentatively shows the presence of two (perhaps three) companions to the main satellite. The restored imagery unambiguously shows the presence of five companions. For the WFS + WD, scenario we are able to see the faint 25 cm targets (see appendix for aberration-free image for comparison) but we also see several artifacts. For the WFS+WD+PD scenario, we have lost the ability to see the 25 cm objects (most likely due to the reduction in the SNR of each individual data frame due to the splitting of the photons for phase diversity) but we find a dramatic reduction in the number of artifacts and the level of the residual halo around the main satellite. That is, using all the available constraints improves the resolution and decreases the probability of false detection. Note, the images are displayed on a logarithmic scale to emphasize the low-level structure.



Figure 7. A demonstration of how extending the observation period improves the detection sensitivity. Here the restored images, at $0.9\ \mu\text{m}$ (left) and $0.4\ \mu\text{m}$ (right), are based on 77 seconds of simulated data including WFS and wavelength diversity measurements. The $25\ \text{cm} \times 25\ \text{cm}$ targets at a distance of 150 m from the main satellite (5 o'clock and ~9 o'clock positions) are now identified with a high degree of confidence (i.e., the probability of false detection is low because the target is clearly detected at two widely separated wavelengths). In addition, the improved resolution at $0.4\ \mu\text{m}$ has enabled the clear detection of an object close to ANIK-F2 at the 9 o'clock position. We have used a logarithmic scale for the images to emphasize the low-level structure. For comparison, we show the undistorted "truth" object in the appendix.

We have developed a novel blind image restoration algorithm to address these issues. To ensure versatility we have designed the algorithm for use with data obtained under a wide range of imaging modalities, including "long-exposure" diversity imaging. By capitalizing on new prior information (spectral holes), and improving the synergy between the data acquisition and image restoration processes (through using wavelength- and temporal phase-diversity channels), we find that we can significantly extend both the level of atmospheric turbulence under which we can produce high-fidelity restorations and the dynamic range of the restorations. Together these improvements provide a potential breakthrough for Space Situational Awareness using the Air Force's 3-meter class telescopes.

References

1. T. J. Schulz, "Multi-frame blind deconvolution of astronomical images," *J. Opt. Soc. Am. A.*, **10**, 1064-1073 (1993).
2. S. M. Jefferies and J. C. Christou, "Restoration of astronomical images by iterative blind deconvolution," *Astrophys. J.*, **415**, 862-874 (1993).
3. R. A. Gonsalves, "Phase retrieval and diversity in adaptive optics," *Opt. Eng.* **21**, 829-832 (1982).
4. H. R. Ingleby and D. R. Mc Gaughey, "Real data results with wavelength-diverse blind deconvolution," *Opt. Lett.* **30**, 489-491 (2005).
5. Milton, M. and Lloyd-Hart, M., "Disk harmonic functions for adaptive optics simulations", in *Adaptive Optics: Analysis and Methods/Computational Optical Sensing and Imaging/Information Photonics/Signal Recovery and Synthesis*, Technical Digest (Optical Society of America, 2005), paper AWA3 (2005).

6. W. H. Press, S. A. Teukolsky, W. T. Vetterling, and B. P. Flannery, *Numerical Recipes in C*, 2nd ed. (Cambridge, U. Press, Cambridge, UK, 1992)
7. D. Gerwe, M. Johnson and B. Calef, "Local minima analysis of phase diverse phase retrieval using maximum likelihood", *Proceedings of the Advanced Maui Optical and Space Surveillance Technologies Conference*, held in Wailea, Maui, Hawaii, September 17-19, 2008, Ed.: S. Ryan, The Maui Economic Development Board, p. E28 (2008)
8. M. C. Roggeman, P. A. Billing and J. Houchard, "Numerical studies of the value of including pupil intensity information in multi-frame blind deconvolution calculations for data measured in the presence of scintillation", *Proceedings of the Advanced Maui Optical and Space Surveillance Technologies Conference*, held in Wailea, Maui, Hawaii, September, 2007, Ed.: S. Ryan, The Maui Economic Development Board (2007)
9. L. M. Mugnier, T. Fusco and J. M. Conan, "MISTRAL: a myopic edge-preserving image restoration method, with application to astronomical adaptive-optics-corrected long exposure images," *J. Opt. Soc. Am. A.*, **10**, 1841-1854 (2004)
10. Johnston, R.A., Connolly, T.J. and Lane, R.G., "An improved method for deconvolving a positive image," *Optics Communications*, **181**, 267-278 (2000)
11. Worden, S. P., Angel, R. A., Lloyd-Hart, M., Hinz, P., Hege, E. K., Jefferies, S. M. and Hope, D. A., "Observing deep-space satellites with the MMT and Large Binocular Telescope", *Proceedings of the Advanced Maui Optical and Space Surveillance Technologies Conference*, held in Wailea, Maui, Hawaii, September, 2005, Ed.: S. Ryan, The Maui Economic Development Board (2005)

Appendix: Details of Numerical Simulations

a) Strong Turbulence Simulation

Turbulence conditions	Kolmogorov turbulence $r_0=4.5$ cm, $\tau_0=8$ msec (at 0.4 μm)
Level of AO correction	30% of first 50 modes (Gives a Strehl of 0.10 at 0.9 μm^{R3} and 0.02 at 0.4 μm)
Telescope aperture	3.65 m
Observing wavelengths	0.88 μm and 0.44 μm
Integration time/frame	8 msec
Total observing time	640 msec
CCD read noise	8 e ⁻
Main target (Linear size, magnitude)	13.2m x 4.2m; mag+3

b) Faint Target Simulation

Turbulence conditions	Kolmogorov turbulence $r_0=15$ cm, $\tau_0=12$ msec (at $0.5 \mu\text{m}$)
Level of AO correction	30% of first 50 modes (Gives a Strehl of 0.10 at $0.88 \mu\text{m}$ and 0.02 at $0.44 \mu\text{m}$)
WFS Data	Measurements of first 50 modes
Telescope aperture	3.65 m
Observing wavelengths	$0.88 \mu\text{m}$ and $0.44 \mu\text{m}$
Diversity phase	± 1 wave of spherical aberration injected as a sinusoidal wave of period 4 secs.
Integration time/frame	384 msec
Total observing time	3secs
CCD read noise	$8e^-$
Main target (Linear size, magnitude)	50m x 5m; mag+9

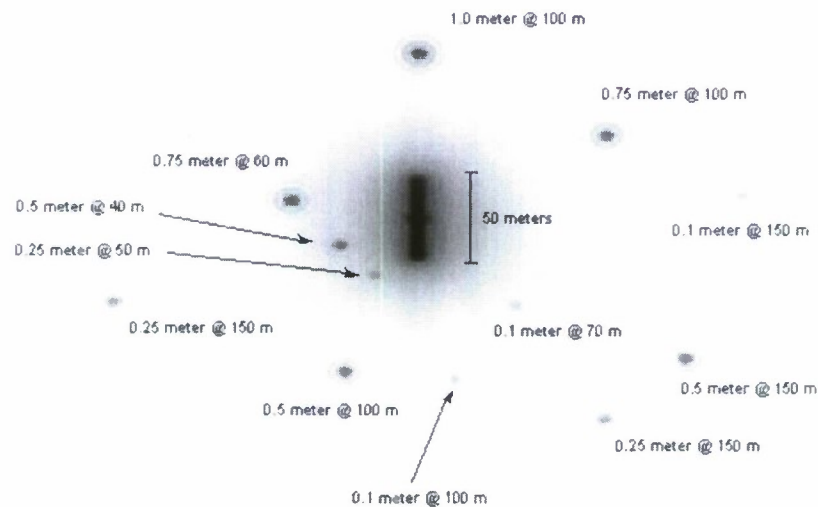


Figure A.1. This shows the diffraction-limited true scene at $0.44 \mu\text{m}$ for the faint target simulation; a model of the communications satellite Anik-F2 surrounded by microsatellites of varying size and distance away. The display scale is logarithmic.